Journal of Materials Chemistry A

Accepted Manuscript

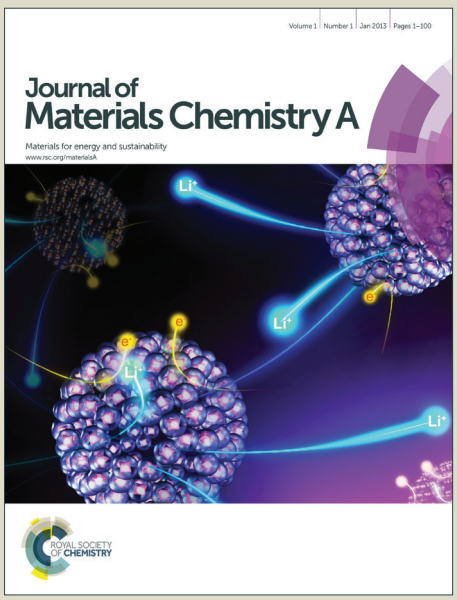

ROYAL SOCIETY OF CHEMISTRY

www.rsc.org/materialsA

Mitigating Capacity Fade by Constructing Highly-Ordered Mesoporous Al_2O_3/Polyacene Double-Shelled Architecture in Li-Rich Cathode Materials

Ming Xu, Zhaoyong Chen*, Huali Zhu, Xiaoyan Yan, Lingjun Li, Qunfang Zhao

School of Physics and Elctronic Science, Changsha University of Science and Technology, Changsha, 410004, Hunan Province, China.

*Corresponding Author: Prof. Zhaoyong Chen, chenzhaoyongcioc@126.com

Abstract

Lithium-rich layered oxides, $xLi_2MnO_3 \cdot (1-x)LiMO_2$(M=Ni, Mn, Co), have been considered as one of the most promising cathode active materials for rechargeable lithium-ion batteries due to the high capacity over 250 mAh g^{-1} between 2.0-4.8V. However, the commercialized application of these cathodes has so far been hindered by their severe capacity fading and transition metal dissolution during high voltage cycling (>4.5 V *vs.* Li/Li^+). To overcome this barrier, a double-shelled architecture consisting of inner conductive polyacene layer and outer mesoporous Al_2O_3 layer is constructed. A polyacene layer with high electron conductivity is first coated on the surface of $0.5Li_2MnO_3 \cdot 0.5LiNi_{0.5}Co_{0.2}Mn_{0.3}O_2$ cathode material, followed by a in-sol treatment combined hydrothermal method to produce highly-ordered mesoporous Al_2O_3 layer. Compared to previous studies, this double-shelled architecture has substantially improved the electrochemical performance of $0.5Li_2MnO_3 \cdot 0.5LiNi_{0.5}Co_{0.2}Mn_{0.3}O_2$ cathode material. Two striking characteristics are obtained for this double-shelled lithium-rich layered oxide cathode material: (1) The electrochemical capacity is greatly improved, reaching to 280 mAh g^{-1} (2.0V-4.8V at 0.1C), (2) the transition from layered phase to spinel is delayed, leading to the superior capacity retention of 98% after 100^{th} cycle.

Keywords: *Lithium-rich layered oxide, Double-shelled architecture, Polyacene, Mesoporous alumina, Cathode materials, Lithium-ion batteries.*

1. INTRODUCTION

Rechargeable lithium-ion batteries (LIBs) have become the main power sources for portable electronic devices due to their high energy density and long cycle life. The fast development of electrified vehicles such as electric vehicles (EVs) and hybrid electric vehicles (HEVs) requires better and smaller LIBs for their energy storage.[1, 2] As a cathode material, $LiCoO_2$ has been widely used in commercialized LIBs due to its suitable energy density and facile synthesis.[3] However, the high cost and dissatisfactory cycle life limit its application in large capacity LIBs such as EVs. As the most promising candidates to replace $LiCoO_2$ cathode material, layered composite materials $LiMO_2$ (M=Ni, Mn, Co) have gradually been applied since Ohzuku *et al.*[4] first reported the $LiNi_{1/3}Co_{1/3}Mn_{1/3}O_2$ cathode material in 2001. Other cathode materials, such as spinel $LiMn_2O_4$ and olivine $LiFePO_4$, have been developed for decades.[5-11] Nevertheless, all of their available discharge capacities approach their limits(<180 mAh g^{-1}), thus cathode materials associated with higher capacities are urgently needed to meet the demand for the further energy density enhancement of LIBs.

Lithium-rich layered oxides (LLMO) that can be represented in two-component notation, $xLi_2MnO_3 \cdot (1-x)LiMO_2$ (M = Ni, Co, Mn), are receiving international attention because they can deliver an exceptionally high rechargeable capacity of 250 mAh g^{-1} between 2.0 V and 4.8 V.[12-17] This high capacity can be achieved because lithium can be removed electrochemically from the $LiMO_2$ component below 4.5V with a concomitant oxidation of the M cations to a tetravalent state, and thereafter, as Li_2O above 4.5 V from the Li_2MnO_3 component.[16] However, this high capacity cathode material still faces challenges:[18-20] 1) Transition metal (TM) dissolution occurs at high electrode potentials (>4.5V *vs.* Li/Li^+), 2) Capacity fading upon repeated cycling, 3) Voltage instability.

To solve these problems, surface coating by various of metal oxides and polymers *et al.*[24-26, 30, 32-33], such as AlF_3,[20] Al_2O_3,[21, 31, 34-35] $LiAlO_2$,[22] $Li_4Ti_5O_{12}$,[23] ZnO,[27] Y_2O_3,[28] CeF_3,[29] have been considered as the most promising method. Among

these coatings, Al_2O_3 is a very stable metal oxide, and surface coating by Al_2O_3 has been known as an effective step to treat different types of cathode materials,[21, 31, 34, 35] such as LiM_2O_4 and $LiCoO_2$ materials [21, 31]. The Al_2O_3 coating layer can act as a protective shell to alleviate the side reactions from the electrolytes and improve the structural stabilities of the cathode materials. So far, many approaches have been applied to obtain the Al_2O_3 coating layer. Several groups have tried to utilize the technique of atomic layer deposition (ALD) [34, 35], which can deposit Al_2O_3 layers onto the cathode films at an atomic-scale precision. However, it is found that the Al_2O_3 layer obtained by ALD is mostly amorphous and therefore could not effectively exclude electrolyte from the surface of cathode materials. Besides, ALD procedure is known to be very expensive, and it is hard to be applied on a large scale. Xu *et al.* [31] have repoted Al_2O_3 coated $LiMn_2O_4$ cathode material using $Al(NO_3)_3$ as the Al sources. They explained that when temperature increases to a higher level (such as 700 and 850℃), the Al_2O_3 coating layer exhibits the well-developed crystallinity. The enhanced electrochemical properties indicate that the HF attack from the electrolyte can be effectively suppressed by this Al_2O_3 crystals coating layer. However, the above-mentioned Al_2O_3 coating layers on the surface of cathode materials usually act as insulating wall and hinder a high rate diffusion of lithium ions (Li^+ ions), resulting in the limited improvement on electrochemical performance.

Conductive polymers, such as polyacene (PAS),[11, 32-33] polyaniline [30] and polypyrrole,[33] have been studied as coating materials because they are electrochemical active and highly conductive. For the PAS coating, Xie *et al.* [11] designed a core/shell compound which is consisted of the spherical $LiFePO_4$ structure coated by PAS. The results show that the electronic conductivity of $LiFePO_4$-PAS composite reachs to 10^1 S cm^{-1}. By our previous report [32], the electrochemical performance of $LiMn_2O_4$ can also be enhanced by PAS coating. Besides, the PAS can be charged and discharged by a redox reaction involving Li^+ ions or counter anions of the electrolyte [33]. However, the PAS will be damaged by direct contact with electrolyte upon cycling due to the interfacial side reactions and HF attack.

In order to improve the conductivity and structural stability of LLMO, herein, we have paid special interest to the construction of a double-shelled architecture consisted of inner ultrathin PAS layer and outer highly-ordered mesoporous Al_2O_3 layer, as schematically illustrated in Figure 1. The inner PAS layer is highly conductive and contributes to the fast electron transportation on the surface of LLMO particles. Moreover, the mesoporous Al_2O_3 layer allow Li^+ ions to diffuse along the pores and through the pore walls, significantly shortening the diffusion path for the Li^+ ions. Besides, the Al_2O_3 layer is highly-ordered and therefore effectively buffers the volume change of core during cycles, at the same time, suppress the HF attack from the electrolyte. On this account, the construction of double-shelled LLMO is expected to be a promising approach to improve the electrochemical performance of cathode materials [36-39].

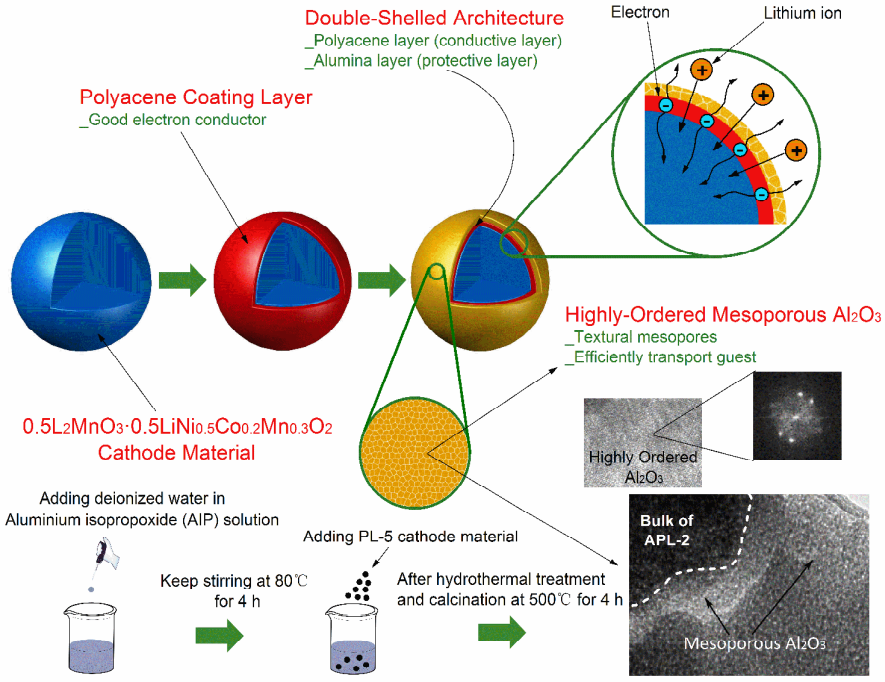

Figure 1 Schematic view of double-shelled architecture consisting of inner PAS layer with high electron conductivity and outer highly ordered mesoporous Al_2O_3 protecting layer. The architecture of the highly-ordered mesoporous Al_2O_3 coating layer is specifically constructed to allow efficient transportation of Li^+ ions, which is

necessary for a long cycle life LIBs.

In this paper, we have demonstrated that the formation of ultrathin PAS layer can enhance the electron conductivity of LLMO, leading to the highly electrochemical capacity of 280 mAh g^{-1} at 0.1C between 2.0V-4.8V. The mesoporous Al_2O_3 layer provides a protecting shell to alleviate the side reactions from the electrolytes, and the cycle life of LLMO cathode material is greatly improved, leading to the superior capacity retention of 98% after 100^{th} cycle.

2. EXPERIMENTAL SECTION

2.1 Sample synthesis

$0.5Li_2MnO_3 \cdot 0.5LiNi_{0.5}Co_{0.2}Mn_{0.3}O_2$ (LLMO) was synthesized by a sol-gel method. Stoichiometric amounts of $C_2H_3O_2Li \cdot 4H_2O$ (99%, Sinopharm Chemical Reagent), $C_4H_6NiO_4 \cdot 4H_2O$ (99%, Sinopharm Chemical Reagent), $C_4H_6CoO_4 \cdot 4H_2O$ (99%, Sinopharm Chemical Reagent), $C_4H_6MnO_4 \cdot 4H_2O$ (99%, Sinopharm Chemical Reagent) were dissolved in deionized water and mixed with a sucrose aqueous solution of 0.5 mol L^{-1} to give the mole ratio of surcrose/metal equal to 1.5. The pH-value was adjusted to 5.0 by addition of nitrate acid, during which nitrate ion provided an in situ oxidizing environment for surcrose being hydrolyzed and converted into carboxylic acids, and the nitrates themselves decomposed to give out brown fumes of nitrogen dioxide. The resulting solution was stirred at 80℃ for 6 h to obtain a clear viscous sol and then dried in an oven at 120℃ for 12 h. The dried precursor was precalcined at 450℃ for 6 h in air to eliminate the organic substances (450℃ precursor) and cooled to room temperature by turning off the furnace. Final crystalline sample was formed by heating the precursor at 900℃ for 12 h in air.

2.2 Surface modification

The as-prepared LLMO (5g) was dispersed by ultrasonication for 1 h in ethanol (40 mL), then 0.25g (0.5g, 1.25g and 1.75g) phenol formaldehyde resin (99%, Wanlong, Dongguan) were added in. This mixture was stirred for 30 min and suspension was then dried at 120 ℃ for 6 h. The acquired powder was annealed at

700 ℃ for 10 min and then quenched in liquid nitrogen with cooling rate of about 300 ℃ min^{-1}. Finally, PAS coated samples (PL-1, PL-2 and PL-5 corresponding to 1 wt. %, 2 wt. %， 5 wt. % and 7 wt. % PAS) was obtained. The coating amount of PAS in composites was analyzed by acid dissolution method. An accurately weighed sample was dissolved in 5 M HCl solution. Then the solution was filtered and washed repeatedly to collect the insoluble residue. Finally, the residue was dried in vacuum for 24 h and carefully weighed. The weight percentages of PAS for PL-1, PL-2, PL-5 and PL-7 were 1.05 wt %, 1.92 wt %, 4.83% and 6.96 wt % respectively.

To prepare the double-shelled LLMO (APL), as schematically illustrated in Figure 1, 0.16g (0.32g, 0.64g) aluminium isopropoxide (AIP) were dissolved in 60 ml anhydrous ethanol and dispersed by ultrasonication for 1 h. Then 50 ml deionized water was added in AIP solution and keep stirring at 80℃ for 4 h to ensure the hydrolysis of AIP. Afterwards, 4.0 g as-prepared PL-5 samples was then added in. The obtained sol was transfered into a 100 ml Teflon-lined stainless steel autoclave. The autoclave was then sealed and maintained at 80℃ for 36 h to obtain the precursor. Final APL-1, APL-2 and APL-4 were obtained by heating this precursor at 500℃ for 4 h, and the Al_2O_3 content corresponds to 1 wt. %, 2 wt. % and 4 wt. %. For comprison, another 4.0 g PL-5 sample was dispersed in anhydrous ethanol and deionized water with strong stirring, then $Al(NO_3)_3 \cdot 9H_2O$ was added into the obtained suspension. The amount of Al in the solution was fixed at 2 wt% of PL-5 sample as Al_2O_3 form. After stirring in air for 12 h, the suspension was evaporated at 80℃, accompanied by a slow evaporation of solvent. Finally, the precursor from above was calcined for 4 h at 500℃ (APL-N_1), 700℃ (APL-N_2) and 850℃ (APL-N_3) respectively.

2.3 Characterization

The crystallographic structure of bare and double-shelled LLMO powders were examined by using a Rigaku D/Max 200PC X-ray diffraction (XRD) with a graphite monochromator and Cu K_α radiation at a scan rate of 5° min^{-1}. Transmission electron microscopy (TEM) images were captured on a JEM-2010 microscopy at an

acceleration voltage of 200 kV, to investigate the characteristics of the polyacene-alumina double coatings. The morphology of the powders was determined by scanning electron microscopy (SEM, Nova NanoSEM-230). The Barret Joyner Halenda (BJH) pore size distribution was characterized by nitrogen adsorption-desorption isotherms (Quadrasorb S1-3MP). To investigate the electronic conductivity, accurately weighed 3.00g samples were added into a steeliness cylinder-shaped mould with diameter of 4.10 cm and pressed under 15 Mpa. Finally, all samples were made into a round pie shape with thickness of 0.14 cm and used to measure the corresponding resistivity via four-point probes method. (Four Point Probing System, RTS-8).

2.4 Electrochemical measurements

Electrochemical performances of the samples were measured using galvanostatic cycling with two-electrode coin cells (type CR2025) between 2.0-4.8 V on Land battery test system (Land CT2001A, Wuhan, China). The electrode was fabricated by coating the slurry of a mixture containing synthesized sample, acetylene black and polyvinylidene difluoride (PVDF) with a weight ratio of 85:10:5 onto circular aluminum foils as current collector. The electrodes were punched into disks with ø=1.0 cm and thickness of 0.025 mm. The active material loading was *ca.* 3.0 mg cm^{-2}. Cells were assembled in an Argon-filled glove box (Etelux LAB2000), using the metallic lithium foil as counter electrode. The electrolyte was 1 M $LiPF_6$ dissolved in ethyl carbonate (EC) and dimethyl carbonate (DMC) (1:1 in volume) and the separator was Cellgard 2400 membrane. The electrochemical impedance spectroscopy (EIS) of the cells was conducted on an electrochemical workstation (Autolab PGSTAT302N) with a frequency range of 1 mHz-100 kHz.

To investigate the microstructure and morphology changes of cathode materials after long-term cycles, the electrodes fully discharged to 2.0V were firstly disassembled from coin cells and rinsed with dimethyl carbonate(DMC) several times in the glove box, and then dried at room temperature. The dried electrodes were applied for HRTEM analysis, the active materials were raked out and dispersed

in NMP. Then they were transferred onto carbon coated Cu grids for further analysis.

3. RESULTS AND DISCUSSION

3.1 Morphology and interface analysis

The SEM image of the 450℃ precursor is shown in Figure 2a. During the calcination at 450℃, the metal ion-chelated complex decompose into CO_2 and H_2O, and a large amount of heat is generated. The amount of gases that escape during combustion prevent the agglomeration of precusor for LLMO sample. The 450℃ precursor exhibits the relatively amorphous morphology compared to the LLMO sample, as shown in Figure 2b. The LLMO sample exhibits obviously visible fringes (inset of Figure 2b), indicating the well-grown crystals. The particle size of LLMO sample is in the range from 300 to 500 nm which is consistent with the report of the LLMO materials [40, 41].

Figure 2c-2h show the morphological characteristics of PL-1, PL-2, PL-5 and APL-1, APL-2, APL-4 samples (PL-7 is shown Figure S3). Compared with the morphological characteristic of bare LLMO particles, obviously visible fringes become gradually obscure for PL-1, PL-2, PL-5 and APL-1, APL-2, APL-4 particles, which is related to the coating of ultrathin PAS layer (Figure 2c-2d, FTIR is employed to identify the PAS, as discussed in following section) and Al_2O_3 coating layer (Figure 2f-2h). However, for the APL-4 sample, aggregated Al_2O_3 sheets (Figure 2h) are formed when increased the Al^{3+} ions concentration corresponding to 4 wt. % Al_2O_3. Excess Al^{3+} ions unhomogeneouly distribute on the surface of particles and grow into Al_2O_3 walls, resulting in the longer path for the transportation of Li^+ ions. As for the APL-1 and APL-2 samples, Al^{3+} ions are homogeneously covered on the particle surface (Figure 2g and corresponding EDS mapping). Figure S1 and Table S1 show EDXS analysis results for the LLMO, APL-1, APL-2 and APL-4 smaples, which indicates that the experimentally measured atomic ratio of Ni, Co and Mn is approximately consistent with the ideal stocihiometry.

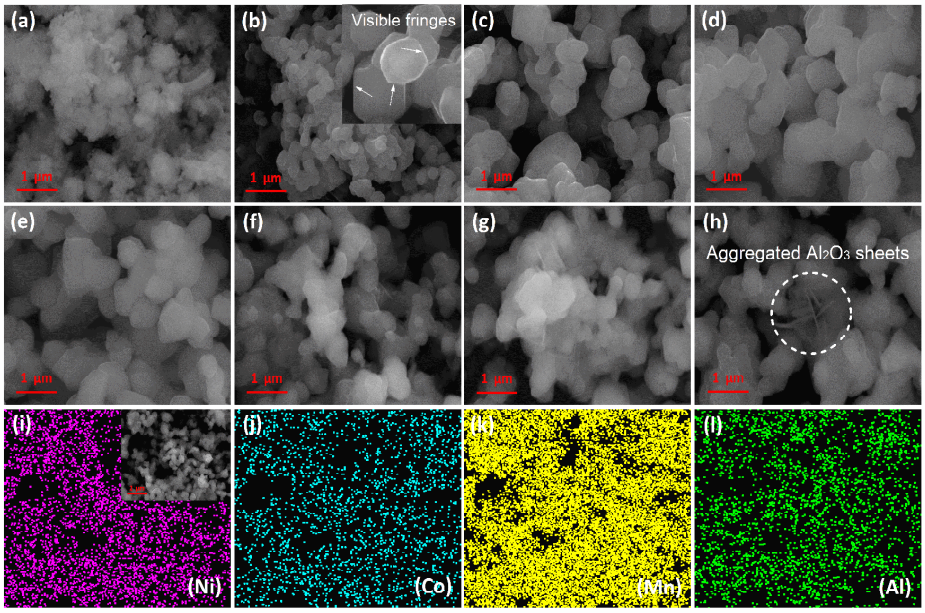

Figure 2 SEM images of 450℃ precursor, bare LLMO material, PAS coated LLMO materials and double-shelled LLMO materials: (a) 450℃ precursor showing the amorphous morphology; (b) bare LLMO sample showing obviously visible fringes; (c)-(e) PL-1, PL-2 and PL-5 samples exhibiting obscure fringes which are related to the coating of ultrathin PAS layer; (f)-(h) APL-1, APL-2 and APL-4 samples showing the characteristics of Al_2O_3 coating layer; (i-l) EDS mapping of APL-2 based on the inset of (i).

HRTEM is performed to study the microstructure of the bare LLMO, PAS coated LLMO and double-shelled LLMO. Figure 3a-3d show the HRTEM images of bare LLMO, PL-1, PL-2 and PL-5 samples. As can be seen in Figure 3a, bare LLMO particles exhibit the smooth surface and show the highly ordered lattice. The HRTEM images in Figure 3b-3d show that the bulk of PL-1, PL-2 and PL-5 particles is covered with an ultrathin PAS layer with an increasing thickness of ca. 2~4 nm (PL-7 is shown Figure S3). As compared to conventional metal-oxide coating which is electronically inert, the distinctive feature of the PAS layer is high electron conductivity (~0.1026 S cm^{-1}). The electron conductivity of PL-5, APL-1. APL-2 and APL-4 samples is measured to be ~7.3283×10^{-6} S cm^{-1}, ~6.2517×10^{-6} S cm^{-1}, ~5.4931×10^{-6} S cm^{-1} and ~1.1784×10^{-6} S cm^{-1} respecticely, which is much higher than

that of bare LLMO sample (~3.1572×10^{-7} S cm^{-1}). The surface electron conductivity of cathode materials is enhanced by wrapping this conductive layer on the surface of PL-5 particles.

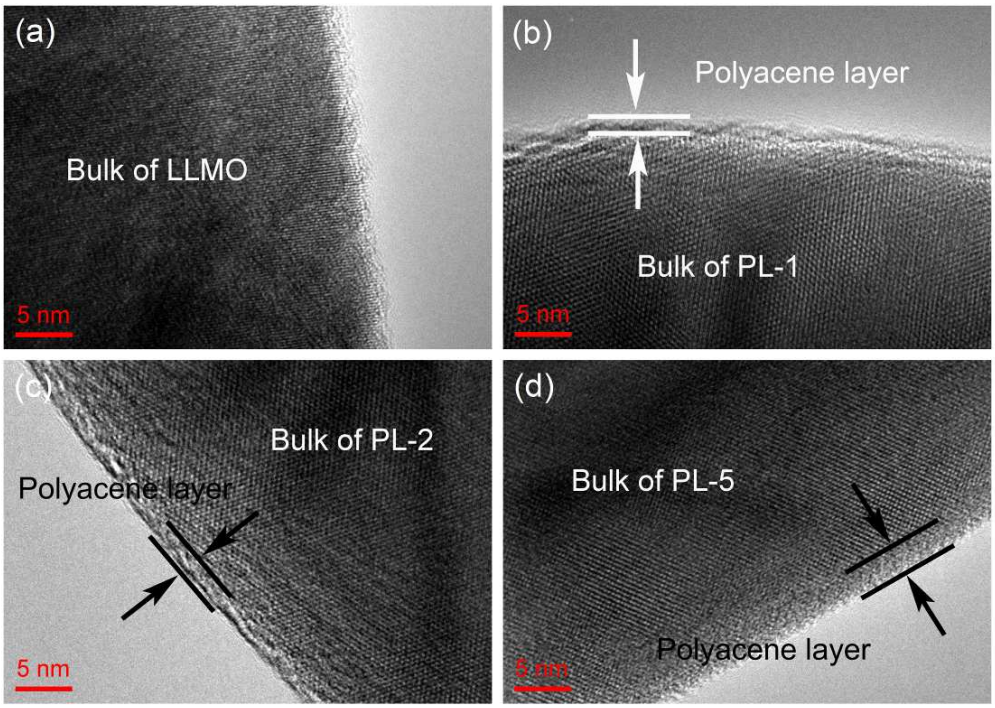

Figure 3 HRTEM images of LLMO, PL-1, PL-2 and PL-5 samples respectively exhibiting the ultrathin PAS layer.

Figure 4a-4i show the representative TEM images of the bare LLMO, APL-1, APL-2 and APL-4 samples. As can be seen in Figure 4b-4d, when a very low AIP concentration (1 wt. % Al_2O_3) is used in the solution, it turns out to be difficult to form a uniform coating on the PL-5 particles, and only discontinuous islands can be observed on the surface (Figure 4b). For increasing AIP concentions (2 wt. % Al_2O_3), we are able to form homogeneously distributed Al_2O_3 layer with a thickness of ca. 20 nm (Figure 4c). The highly-ordered Al_2O_3 layer is mesoporous, which is favorable for Li^+ ions transportation [38]. For APL-4 sample (Figure 4d), the thickness of mesoporous Al_2O_3 layer is about twice than that of APL-2 sample, and the mesoporous Al_2O_3 layer aggregated around the APL-4 particles. These results confirm that increasing the AIP concentration (4 wt. % Al_2O_3) during in-sol treatment, the excess Al^{3+} ions aggregate

and finally form the mesoporous Al_2O_3 sheets. This observation is consistent with that in SEM image (Figure 2h).

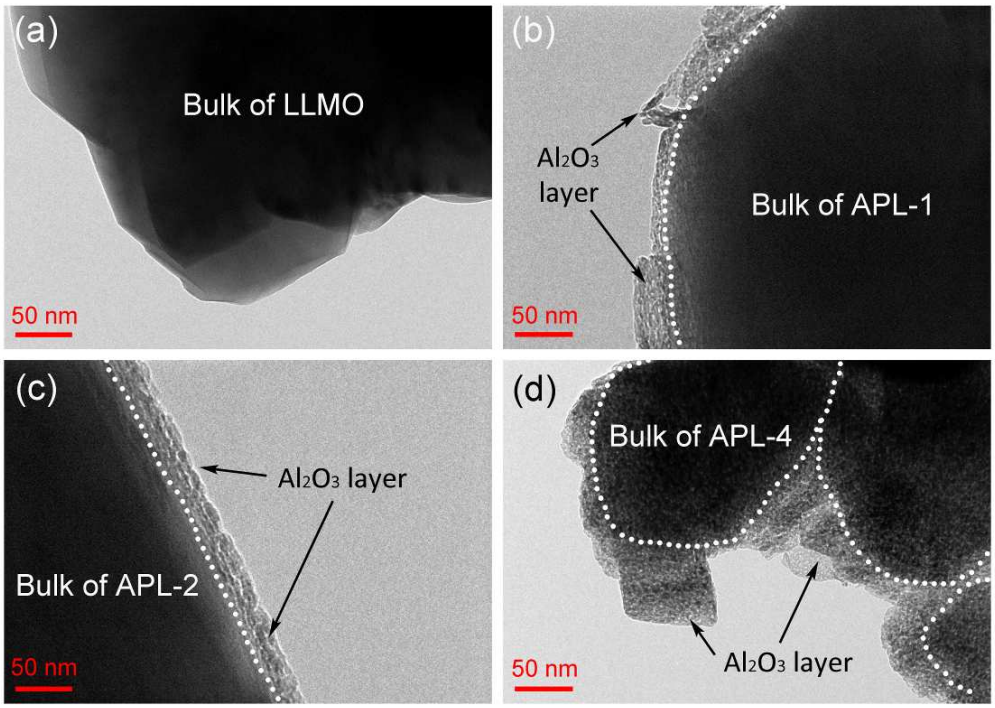

Figure 4 TEM images of (a) LLMO, (b) APL-1, (c) APL-2 and (d) APL-4 samples showing the mesoporous Al_2O_3 layer.

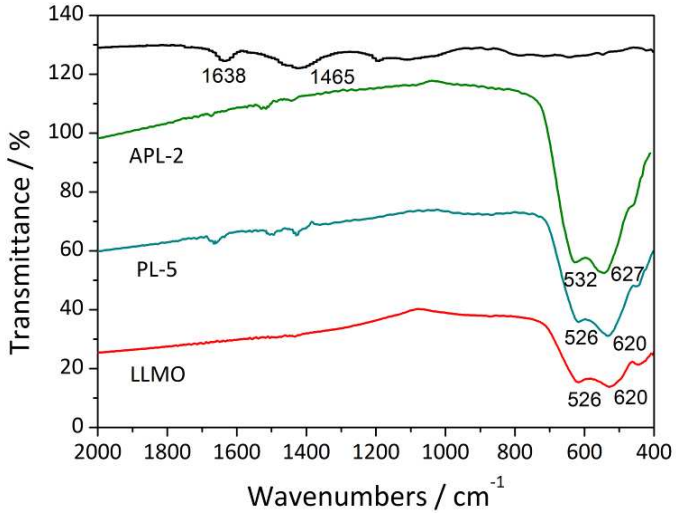

Figure 5 FTIR spectra of PAS, bare LLMO, PL-5 and APL-2 samples: PAS and PL-5 samples show the =CH in-plane deformation vibrations at ca. 1465 cm^{-1} and C=O stretching vibrations at ca. 1638 cm^{-1}; Absorption peaks at 500-700 cm^{-1} are

M-O stretching vibration.

Fourier Transform Infrared Spectroscopy (FTIR) is performed to identify the PAS coating layer. Figure 5 shows the result of FTIR for PAS, LLMO, PL-5 and APL-2 samples. As can be seen in Figure 5, IR spectra of PAS exhibits the peak at 1465 cm^{-1} and 1638 cm^{-1} which are in reference to =CH in-plane deformation vibrations and C=O stretching vibrations, respectively [11, 32]. It is noted that it still retains the C=O and =CH peaks for PL-5 and APL-2 samples, indicating that the dehydration and dehydrocyclization will take place between the molecules of phenolic resin at 700℃ [11] and finally form the PAS layer on the surface of PL-5 particles. Two distinct absorption peaks (500-700 cm^{-1}) caused by the M-O (M=Ni, Co, Mn) stretching vibration are observed in all samples. Obviously, the M-O stretching bands of the APL-2 sample shift from 620 and 526 cm^{-1} to 627 and 532 cm^{-1}, respectively. The shift is due to more Al^{3+} ions diffusing into the LLMO particles at the calcining temperature of 500℃. The diffusing of Al^{3+} ions into the LLMO could decrease the average bond length of M-O[31].

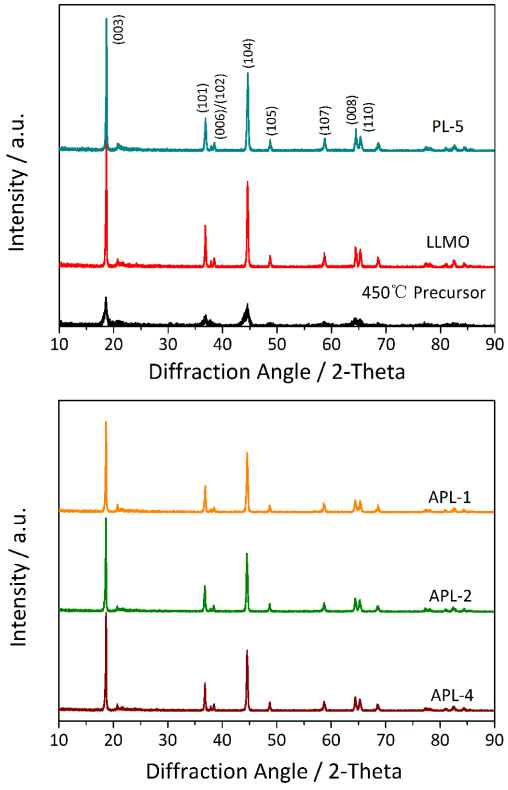

Figure 6 Calibrated XRD patterns of 450℃ precursor, bare LLMO, PAS coated LLMO material: PL-5 sample, and double-shelled LLMO materials: APL-1, APL-2 and APL-4 samples.

Figure 6 shows the powder X-ray diffraction (XRD) patterns of the 450℃ precursor, pure LLMO, PL-5 and APL-2 samples. The XRD patterns of PL-1, PL-2 and PL-7 samples are presented in Support Information (Figure S2). Most of the diffraction peaks can be indexed based on a layered structure with both rhombohedral symmetry (R-3m) and monoclinic structure (C/2m) [12, 13, 18]. Complete splitting of the pair reflections (006)/(102) and (018)/(110) indicates the formation of a typical layered structure for all materials. The integrated intensity ratio of the (003) and (104) lines in the XRD patterns is >1.4 for all samples, indicating the suppressed cation mixing[13, 17, 18]. The (020) reflection within the 2θ range 20-25° is the characteristic of the integrated monoclinic Li_2MnO_3-like component (C2/m) and the Li cation ordering in the TM layer [12, 18]. The lattice parameters of samples calculated from the diffraction data are shown in Table 1. It is interesting to conclude that the lattice volume of APL series samples is smaller than that of the LLMO and PL-5 samples owing to the diffusion of Al^{3+} ions into the surface lattice of APL series samples at high calcining temperature. The ion radius of Al^{3+}(0.53 Å) is smaller than that of Ni^{2+}(0.70Å), Co^{3+}(0.61Å) and Mn^{4+}(0.54Å), thus the substitution by Al^{3+} reduces the lattice volume of APL series samples [31, 35].

Samples	Lattice parameter / Å				$I_{(003)}/I_{(104)}$
	a	c	v	c/a	
LLMO	2.8667	14.2774	101.46	4.9804	1.5033
PL-5	2.8674	14.2763	101.54	4.9788	1.4714
APL-1	2.8571	14.2469	100.72	4.9865	1.4727
APL-2	2.8564	14.2367	100.60	4.9841	1.4830
APL-4	2.8535	14.2351	100.38	4.9887	1.4932

Table 1 Lattice parameter a, c, v and ratios of c/a, $I_{(003)}/I_{(104)}$ for samples calculated from the refined data.

3.1.1 Identification of double-shelled architecture

To identify the double coating layers, HRTEM image of APL-2 smaple is presented in Figure 7. It is noted that this distinct architecture consists of Al_2O_3 layer and PAS layer, forming the double-shelled architecture as vividly illustrated in Figure 1. As shown in Figure 7, the bulk of APL-2 particle shows the typical layered structure with interplanar spacing of 0.475 nm corresponding to (003) plane of the layered structure. The interface of LLMO bulk is closely wrapped by an ultrathin PAS layer with thickness of ca. 4 nm, and the outer surface is the Al_2O_3 layer. It should be noted that the inner PAS layer is highly conductive, contributing a lot to the improvement of electrochemical capacity of LLMO cathode material. The structure characteristic of the outer Al_2O_3 layer looks interesting. The Al_2O_3 layer is highly-ordered with the interplanar sapcing of 0.349 nm corresponding to (210) plane of Al_2O_3 (JCPDS no. 50-1496). Furthermore, compared to the Al_2O_3 coating layer in previous reports[31, 35], it should be noted that this conformal Al_2O_3 layer has mesoporous structure, indicating the the efficient transportation of Li^+ ions. During the redox reaction process in electrode, the inner electrons must pass through outer Al_2O_3 protecting layer to the surface of another particle, finally to collector. As the Al_2O_3 layer is nano-sized, the electron transport throuth Al_2O_3 layer follows the electron tunneling mechanism which explains the electron transport behavior in dielectric metal oxide[36, 37].

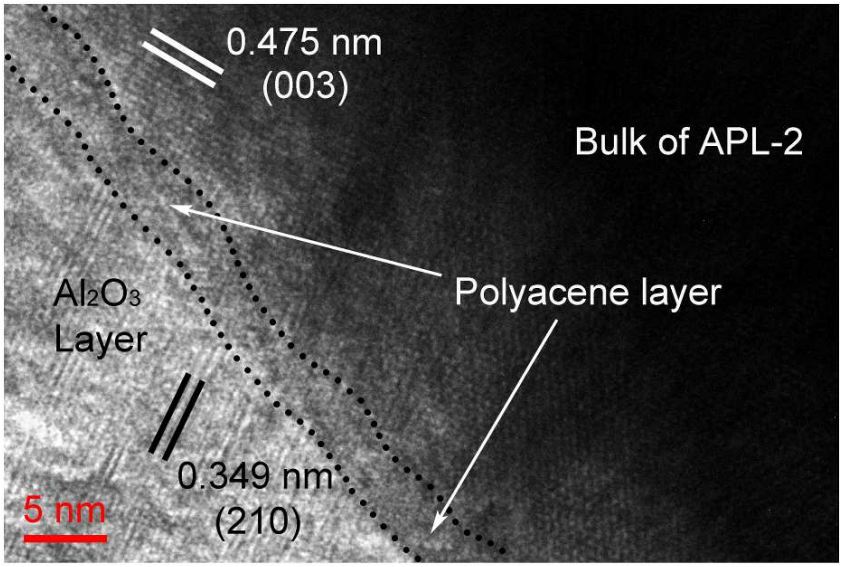

Figure 7 HRTEM image of APL-2 sample showing the interface between bulk of LLMO, PAS and Al_2O_3 layer.

3.1.2 Formation of mesoporous structure

According to previous report [21, 31, 34], although the cathode materials are effectively protected from the errosion effect of electrolyte by dense Al_2O_3 coating layer on the surface, the transportation of Li^+ ions is partially hindered due to the intrinsic insulation of Al_2O_3. The occurrence of mesoporous structure in Al_2O_3, which consists of textural mesopores and intrinsic interconnected pore systems is important and useful for the efficient transportation of guest species to framework binding sites [38, 39]. The highly-ordered mesoporous Al_2O_3 coating layer is specifically designed to allow efficient transportation of Li^+ ions, which is necessary for a long cycle life LIBs.

The structure of mesoporous was usually designed via the evaporation of CO_2 and H_2O during the course of the decomposition of organic templates. [38, 39] In our experiments, the mesoporous Al_2O_3 is obtained via in-sol treatment combined hydrothermal method. The deionized water is added to ensure the formation of $Al(OH)_3$ sol by the hydrolysis of AIP($C_9H_{21}AlO_3$). The detailed chemical mechanisms of the hydrolysis reaction are presented in Support Infomation. After adding PL-5 powders into the $Al(OH)_3$ sol with constant stirring, the $Al(OH)_3$ might migrate on the

surface of PL-5 priticles to form the coating layer. Afterwards, the formation of $Al(OH)_4^-·H_2O$ coating layer is accomplished during hydrothermal treatment. Then the densification and gelation of the precursor sol occurs with the evaporation of ethanol during the various aging periods. After decomposition of the gel by calcining at 500℃ for 4 h, the highly-ordered mesoporous Al_2O_3 coating layer is formed via the evaporation of H_2O.

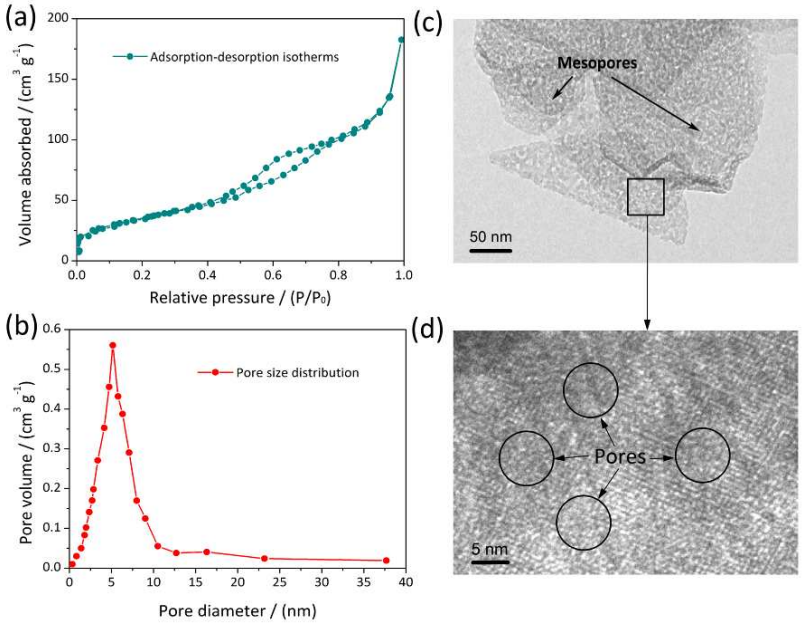

Figure 8 (a)-(b) N_2 adsorption-desorption isotherms and BJH pore size distribution from the adsorption branch isotherm; (c)-(d) TEM and HRTEM images of mesoporous Al_2O_3 obtained via in-sol treatment.

Figure 8 shows the the N_2 adsorption-desorption isotherms and the BJH pore-size distribution of APL-2 sample. The curve exhibits a typical characteristic of mesoporous materials. The isotherm in Figure 8 has a hysteresis loop due to capillary condensation of N_2 gas in the pore. The BJH average pore diameter is 5.26 nm for APL-2 sample. Combined the observation in Figure 4b-4d, this Al_2O_3 layer has mesoporous structure.

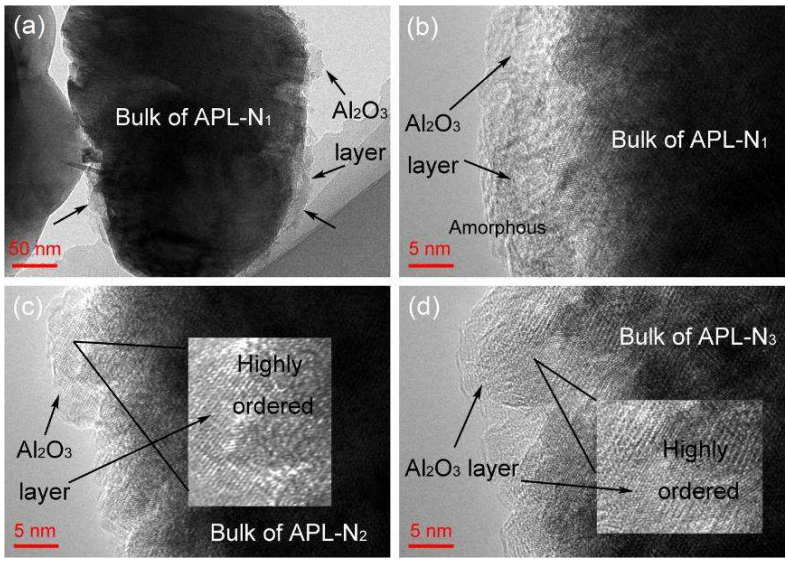

Figure 9 TEM and HRTEM images of Al_2O_3 coated LLMO materials using $Al(NO_3)_3$ as Al source: (a) TEM image of APL-N_1 sample showing the obvious Al_2O_3 layer on the surface of APL-N_1 particle; (b) HRTEM image of APL-N_1 material based on (a) showing the amorphous Al_2O_3 layer; (c)-(d) HRTEM images of APL-N_2 sample (calcining at 700 ℃) and APL-N_3 sample (calcining at 850 ℃) respectively exhibiting the ordered Al_2O_3 layer.

For comparison, the TEM images of APL-N_1, APL-N_2 and APL-N_3 samples are shown in Figure 9a-9d. As reported [31], the $Al(NO_3)_3$ can be used as Al source to obtain the Al_2O_3. For APL-N_1 sample, Figure 9a and Figure 9b show the Al_2O_3 layer on the surface of particles. This Al_2O_3 layer is relatively amorphous. For APL-N_2 and APL-N_3 samples, it is observed in Figure 9c and 9d that the Al_2O_3 layer exhibits well-developed crystallinity by calcination at 700℃ and 850℃. However, compared to the mesoporous Al_2O_3 layer, the Al_2O_3 layer on the surface of APL-N_1, APL-N_2 and APL-N_3 particles exhibits an "insulator wall", resulting in the limited improvement in electrochemical properties of LLMO.

3.2 Electrochemical performance

3.2.1 Initial charge and discharge capacity

Figure 10a shows the charge and discharge voltage profiles of the bare LLMO, PL-5, APL-1, APL-2 and APL-4 samples measured between 2.0 and 4.8 V at 0.1C rate

at room temperature. A representative profile of LLMO which is composed of a sloping curve below 4.5 V and a long plateau around 4.5 V in the first charge process can be seen clearly [14-18]. In addition, the long plateau (at 4.5 V) disappeared in the second charge process (Figure 10b), which indicates that the removal of "Li_2O" in the first charge process is irreversible [16, 17].

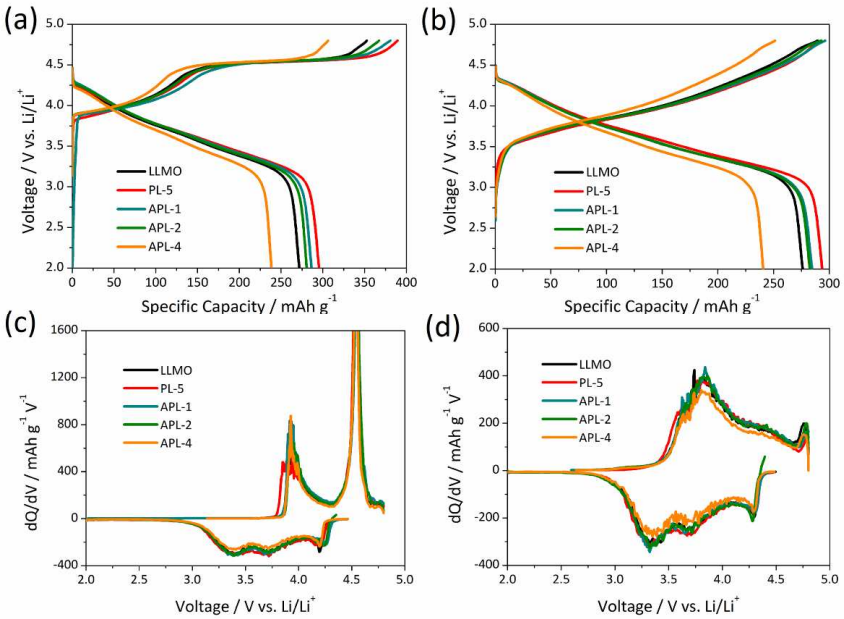

Figure 10(a)-10(b) Initial and second voltage profiles of bare LLMO, PL-5, APL-1, APL-2 and APL-4 samples between 2.0 and 4.8 V at 0.1 C (=20 mA g^{-1}); 10(c)-10(d) the corresponding differential capacity (dQ/dV) vs. cell potential profiles.

The bare LLMO sample shows the initial discharge capacity of 274 mAh g^{-1}, while PL-5 and APL-1, APL-2, APL-4 samples exhibit 295 mAh g^{-1}, 286 mAh g^{-1}, 280 mAh g^{-1} and 238 mAh g^{-1} respectively. As expected, the PL-5 sample delivers higher capacity than the bare LLMO sample (the initial charge and discharge voltage profiles of PL-1, PL-2 and PL-7 samples are presented in Figure S4). This is due to the high electron conductivity of PAS coating layer on the surface of PL-5 particles. Moreover, as reported, the PAS can be charged and discharged by a redox reaction involving Li^+ ions or counter anions of the electrolyte [33]. Figure 10c-10d present the dQ/dV curves of all materials after 1st and 2nd cycle respectively. As can be seen in Figure 10c, two distinct oxidation peaks at approximately 3.8 and 4.5 V of the initial

dQ/dV curves are observed in all materials. The peak around 3.8 V is due to the oxidation of $Co^{3+/4+}$ and $Ni^{2+/3+/4+}$. The peak at 4.5 V is due to the irreversible electrochemical activation reaction of Li_2MnO_3 [46]. Whereas, the dQ/dV curves of the composites show three reduction peaks at ca. 3.3 V, 3.75 V and 4.3 V. The reduction of Mn^{4+} in the layered MnO_2 component occurs initially at ca. 3.3 V. The peaks near 3.75 V and 4.3 V are related to the reaction of $Co^{4+/3+}$ and $Ni^{4+/2+}$.[46]

3.2.2 Cycling performance and rate capability

The variation of discharge capacity as a function of cycle number is performed to evaluate the capacity retention of the bare LLMO, PL-5, APL-1, APL-2 and APL-4 samples (cyclic performance of PL-1, PL-2 and PL-7 samples is shown in Figure S5). Detailed comparison discloses that the APL-2 sample exhibits significantly reduced capacity decay, indicating the delay of layered to spinel-like phase transition. As can be seen in Figure 11a, the capacity loss of the APL-2 sample is only 2 % after 100^{th} cycles at 0.2C rate between 2.0-4.8 V, while the bare LLMO and PL-5 samples suffered 26 % and 15 % capacity loss respectively after 100^{th} cycles. Figure 11b shows the cyclic performance of all materials at 1C rate. It is noted that the APL-2 sample shows the excellent capacity retention with 95 % after 100^{th} cycle, which is much superior than the 64 % observed for bare LLMO sample. The superior capacity retention of the APL-2 sample is ascribed to the double-shelled architecture which functions as a protective layer to reduce the oxidative decomposition of the electrolyte at high voltage (>4.5 V *vs.* Li/Li^+), such that the structural stability of cathode material can be enhanced.

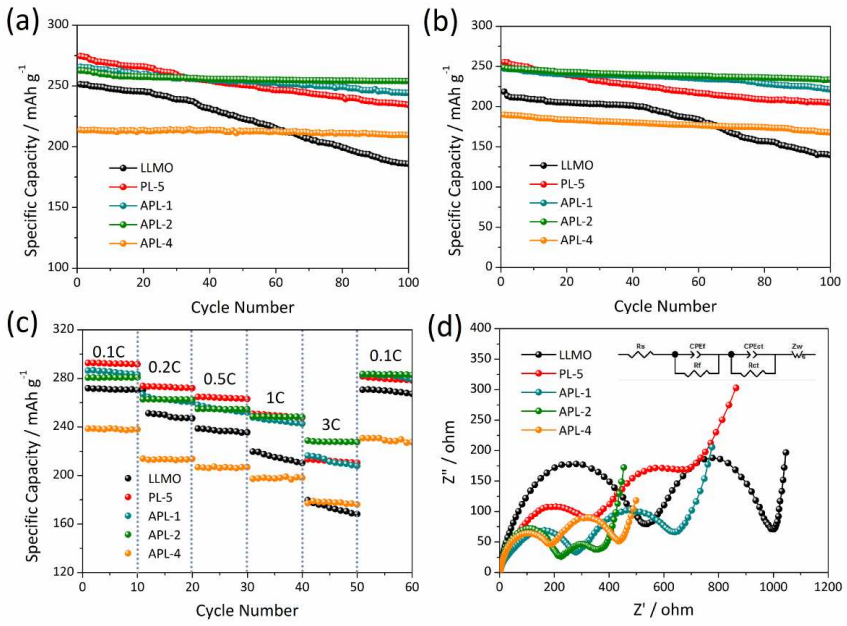

Figure 11 (a) Cycle performance during 100th cycle between 2.0 and 4.8 V at 0.2C; (b) Cycle performance during 100th cycle between 2.0 and 4.8 V at 1C; (c) Rate capabilities from 0.1 C to 3 C between 2.0 V and 4.8 V. (f) Nyquist plots of all electrodes after 100th cycle. Frequency range: 1×10^{-3}Hz - 1×10^{4} Hz.

The charge and discharge measurements on all of the samples are conducted at 0.1 C, gradually increased to 3 C, and finally returned back to 0.1 C, as shown in Figure 11c. At a low current rate of 0.1C, 0.2C and 0.5C, the double-shelled samples do not show much of an advantage over the pristine one. When the current rate is increased to 1C, the APL-2 sample can deliver a capacity of 248 mAh g^{-1}, while it is only 220 mAh g^{-1} for the LLMO sample. At higher current rates such as 3C, the PAS coated sample and double-shelled samples show the better rate capability than the LLMO sample, especially for the APL-2 sample. This is due to the fast ionic and electronic passways on the surface region of APL-2 sample. Obviously, the APL-4 sample shows a very low capacity, because the thick and aggregated Al_2O_3 layer is not appropreciate for improving the capacity. Combined with the SEM and interface analysis, we are able to assume that the textural mesopores and intrinsic interconnected pore system forms when the mass fraction of Al_2O_3 is ranging from 2 wt.% to 4 wt.%. When excess AIP is added such as 4 wt.% Al_2O_3, the aggregated

Al_2O_3 layer prolong the lithium-ion pathway toward the active cathode. Furthermore, it cannot effectively enhance the electronic conductivity and has no contribution to the stabilization of layered structure, even at high current rate. Besides, a drastic fall in the specific capacity at 3 C is observed for LLMO sample, which is attributed to the dissolution of transition metals by HF attack, and electrolyte decomposition may cause a rapid increase of the interfacial resistance thereby accelerating the capacity loss as cycling progresses. With double-shelled architecture applied, the active cathode is well protected and the polarization at the high rate decreases for APL-2 sample.

To understand the beneficial effect of double-shelled architecture on the electrochemical performance of LLMO materials, Electrochemical Impedance Spectroscopy (EIS) measurements are carried out after 100^{th} cycles at 0.2C and the corresponding Nyquist plots are shown in Figure 11d. A significant decrease in the area of the semicircle, which reflects the charge-transfer resistance (R_{ct}), is observed for APL-2 sample. The depressed semicircle in the high frequency regions is related to the resistance from SEI film on the active material (R_f). An equivalent circuit used to fit the spectra is shown in the inset. Upon cycling, a significant increase in the R_f is observed for bare LLMO sample, indicating the increased interficial resistance during cycling. As expected, for bare LLMO sample, this is believed to arise from the damage of the materials surface contributed to the severe side reactions at the interface between the electrode and the electrolyte during high voltage cycling. R_{ct} is calculated as 221 Ω, 183 Ω, 232 Ω, 316 Ω and 425 Ω for the APL-1, APL-2, APL-4, PL-5 and bare LLMO samples. The enhanced electron conductivity of PL-5 sample facilitates the transfer of electrons from the current collector to the cathode material, thus reducing the resistance after cycling. Moreover, the Li^+ ions diffusion coefficient of APL-2, PL-5 and bare LLMO samples is calculated to be 7.24×10^{-12} cm^2 S^{-1}, 2.28×10^{-12} cm^2 S^{-1} and 5.83×10^{-13} cm^2 S^{-1} respectively. The enhanced Li^+ ions diffusion is definitely ascribed to the unique mesoporous Al_2O_3 layer which allows efficient transportation of Li^+ ions.

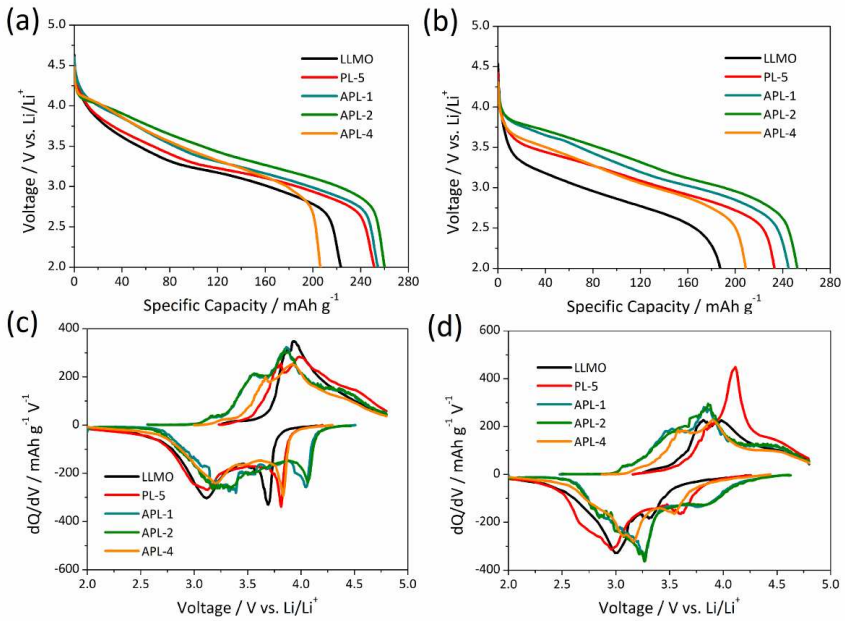

Figure 12 (a)-(b) Discharge curves of all samples after 50th cycle and 100th cycle; (c)-(d) the corresponding differential capacity (dQ/dV) vs. cell potential profiles.

Figure 12a presents the discharge profiles of the bare LLMO, PL-5, APL-1, APL-2 and APL-4 samples after 50th cycle show obviously different voltage decay. The voltage decay is extremely serious for bare LLMO and APL-4 samples. The significant voltage decay could be attributed to two reasons: 1) the deterioration of the electrode/electrolyte interface owing to the attack by the acidic species in the electrolyte and the continuous accumulation of a SEI layer on the electrode surface associated with parasitic side reactions between the electrode and the electrolyte [19, 20], 2) the intrinsic phase transformation from layered to spinel-like structure during the activation of the Li_2MO_3 component in the initial charge process and during each charge to high voltage in the subsequent cycles [20, 42-44].

Compared to the rapid decrease in the average discharge voltage of LLMO sample (from 3.42 V to 2.90 V after 100th cycle at 0.2C), the PL-5 and APL-2 samples display a gradually enhanced values from 3.40 V to 3.11 V and 3.41 V to 3.15 V respectively. It is obviously observed that the voltage decay has been delayed by the double-shelled architecture. Figure 12c-12d present the dQ/dV curves of all materials after 50th and 100th cycle respectively. However, the reduction peaks of the bare

LLMO, PL-5 samples continuously shifted to a lower voltage of 3.0 V upon cycling. This lowering of the voltage with extended cycling might be related to surface structural changes that are thought to occur due to repeated high-voltage cycling (>4.5 V *vs.* Li/Li^+) [44-47]. While the reduction peaks corresponding to the layered structure still centers in 3.3 V after 100^{th} cycle. From the aspect of electrochemistry, electrode polarization, owing to the poor kinetics, brings about the over-gain and over-loss of electron, leaving the active materials suffering from an over-reduction or over-oxidation state[24]. With improvement effect on reaction kinetics, the double-shelled architecture reduces the polarization so that the cathode can react under a more equilibrium state. So a better cycling stability is obtained, indicating that the double-shelled architecture is very effective to delay the phase transition during cycling.

3.3 Delayed phase transition in double-shelled architecture upon cycling

In order to study the structural evolution of bare LLMO, PL-5 and APL-2 samples upon cycling, HRTEM and FFT imaging are performed. Figure 13a-13c present the HRTEM images of bare LLMO sample after 10^{th} cycle, 50^{th} cycle and 100^{th} cycle repectively. As can be seen in Figure 13a and corresoponding FFT, the distortion region is observed over distances of ca. 5 nm from the surface after 10^{th} cycle. The FFT in inset of Figure 13a exhibits a spinel-like phase (space group *Fd-3m*). In the maintime, the bulk region of 10^{th} cycled LLMO sample still remains layered phase. The clear evidence observed for 10^{th} cycled LLMO sample shows that the evolution in the structure is mainly localized on the surface at early cycled stage [42]. Formation of spinel-like phase at the surface region of cycled LLMO sample is ascribed to the transition from layered structure to spinel [43, 47]. This transition is accomplished through the migration of TM ions to the Li sites without breaking down the lattice, leading to the formation of mosaic structured spinel grains within the parent particle, as illustrated in Figure 14. Figure 13b shows that the identified spinel-like structure has been found in the bulk of 50^{th} cycled LLMO sample. In addition to the above observations, significant etching of the particle

surface is detected from 100th cycled LLMO sample (Figure 13c). Without surface coating, the oxygen vacancies formed during the extensive removal of lattice oxygen at high voltage could not be well maintained, leading to densification/shrinkage of the structural lattice. Severely etched particles may finally become fragmented pieces and no longer be available for reversible lithium ion insertion/extraction, resulting in capacity degradation. More important reason is the continuous attack of the particle surface by the acidic species in the electrolyte. Such structrue distortion is responsible for the capacity fade of LLMO sample during repeated charge and discharge cycles at high voltage. In the case of cycled PL-5 sample, as seen in Figure 13d, we have found that this single PAS layer can not suppress or delay the phase transition during cycling. The layered to spinel phase transition still occurs in the bulk region of PL-5 particles. Besides, cracked PAS layer has been found to exist as evidenced by the results of HRTEM imaging in the cycled PL-5 sample. The phase transition, cracked surface coating layer and lattice break-up explain the capacity decay of PL-5 sample upon cycling.

Figure 13e-13f show the HRTEM and corresponding FFT results of double-shelled APL-2 sample. After 100th cycle, we have found that the surface region of cycled APL-2 sample still remain in the rhombohedral phase, which is in good accordance with the better maintained discharge capacity upon cycling (Figure 11a and 11b). This observation likely indicates that the phase transition from layered to spinel can be delayed by this double-shelled architecture.

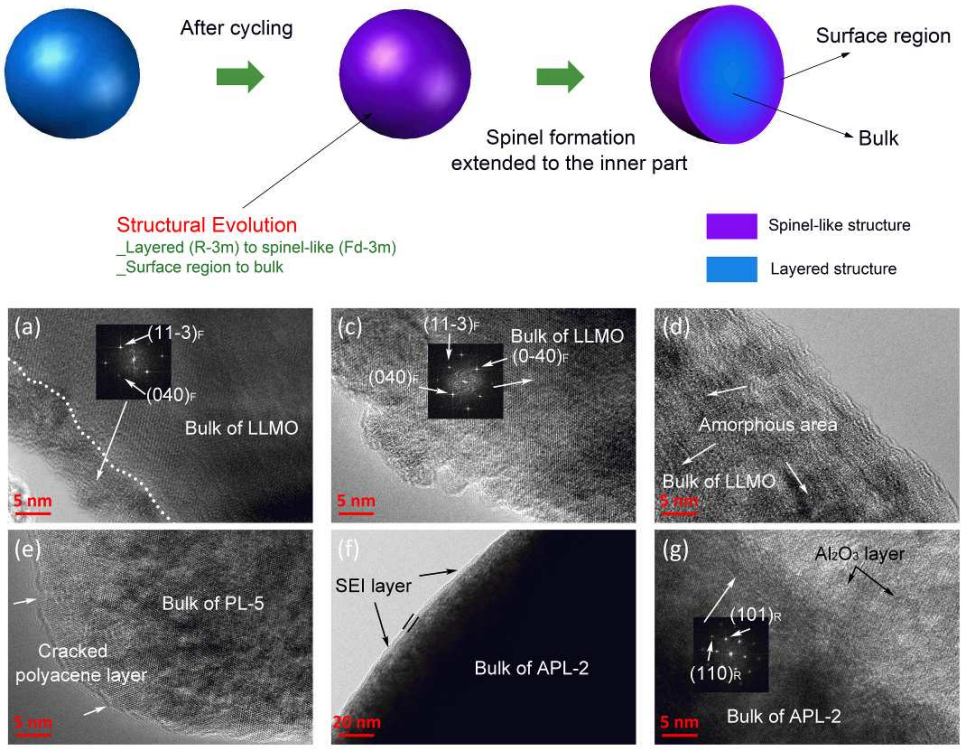

Figure 13 Schematics of structural change from the layered phase to the spinel-like phase during the charge and discharge cycles. HRTEM images of: (a)-(c) the LLMO material after 10th, 50th and 100th cycle; (e) 100th cycled PL-5 sample and (f-g) APL-2 sample after 100th cycle; The indexe marked by subscript R and F is realated to the rhombohedral (R-3m) phase and Cubic (Fd-3m).

Based on the analysis of XRD, TEM and FTIR, a little Al^{3+} ions diffuse into the surface lattice of APL-2 particles when the calcining temperature increases to 500 ℃. These Al^{3+} ions dope into the structure to form a $LiM_{1-x}Al_xO_2/LiMO_2$(M = Ni, Co, Mn) core. Also, it indicates a strong interaction between Al_2O_3 and the host structure. The structure stability of APL-2 sample is enhanced, thus delaying the phase transition during repeated charge and discharge process. Furthermore, the double-shelled architecture can effectively suppress the HF attack and protect the active cathode from an over-reduction or over-oxidation. As a result, the LLMO materials with highly-ordered mesoporous Al_2O_3/PAS double-shelled architecture are very promising for use in high energy density LIBs for large-scale practical applications. The fundamental research works in this paper also provides new perspective on the design

and development of other functional materials with significantly enhanced stability.

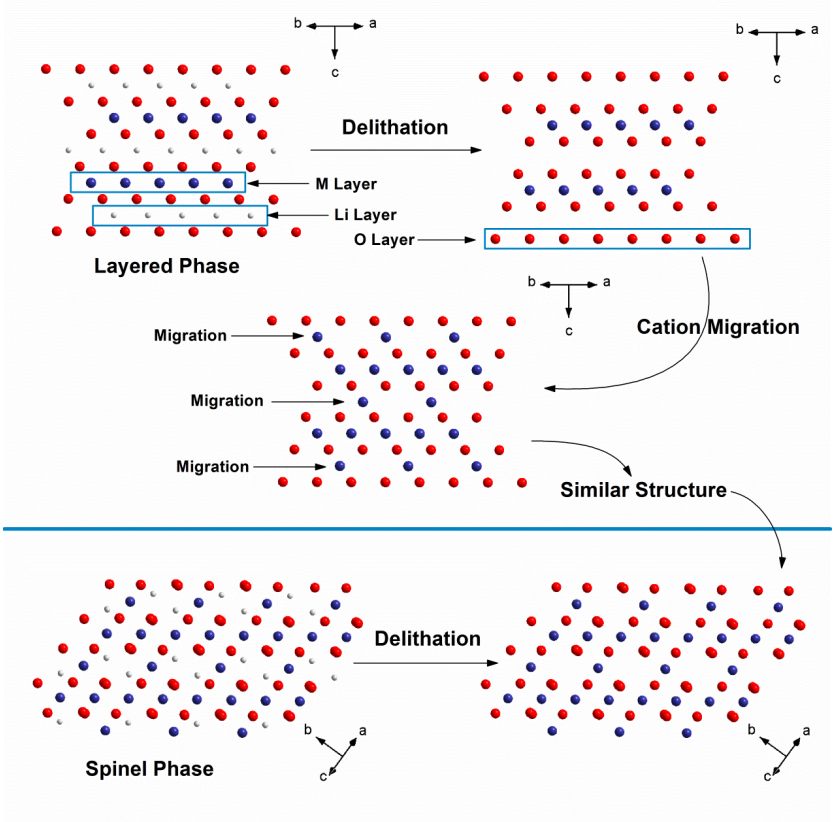

Figure 14 Schematic view of structural evolution from layered structure to spinel-like upon cycling

4. CONCLUSION

In this paper, we proposed a double-shelled $0.5Li_2MnO_3 \cdot 0.5LiNi_{0.5}Co_{0.2}Mn_{0.3}O_2$ cathode material which consists of the inner conductive polyacene layer and outer mesoporous Al_2O_3 layer. This unique double-shelled architecture enhances the electrochemical performance of LLMO cathode material, at the same time, buffers the volume change of core during cycles. We demonstrate that the formation of untrathin polyacene layer can improve the electronic conductivity of LLMO, reaching to the high electrochemical capacity of 280 mAh g^{-1} at 0.1C between 2.0V-4.8V. The mesoporous Al_2O_3 layer which is obtained by in-sol treatment provides a protecting shell to alleviate the side reactions from the electrolytes, and the cycle life of LLMO cathode material is greatly improved, leading to the superior capacity retention of

98% after 100th cycle. The bulk and surface structures of cycled materials are characterized by HRTEM and FFTs. The layered-to-spinel transition is delayed by the compact and continuously distributed surface coating layer. Therefore, the double-shelled architecture provides a strategy to overcome the drawbacks of the LLMO materials and this leads to the extension of the understanding of its structural stability and an improvement method.

ACKNOWLEDGMENTS

The authors gratefully acknowledge the financial support of the Scientific Research Foundation for the Returned Overseas Chinese Scholars of State Education Ministry (No. [2011]1139), the Hunan Provincial Key Laboratory of Materials Protection for Electric Power and Transportation (No. 2013CL07), Changsha University of Science & Technology, PR China, the National Natural Science Foundation of China (No. 51304031), the Hunan Provincial Natural Science Foundation of China (no. 14JJ3089), Scientific Research Fund of Hunan Provincial Education Department (no. 12C0001) and National Undergraduate Innovative Test Program of China.

REFERENCES

1 N. Terada, T. Yanagi, S. Arai, *J. Power Sources*, 2001, **100**, 80.

2 T. Horiba, K. Hironaka, T. Matsumura, *J. Power Sources*, 2003, **119**, 893.

3 M. K. Jo, S. K. Jeong, J. Cho, *Electrochemistry Communications*, 2010, **12**, 992.

4 T. Ohzuku, Y. Makimura, *Chemistry Letters*, 2001, **30**, 642.

5 M. M. Thackeray, P. J. Johnson, *Mat. Res. Bull.*, 1984, **19**, 179.

6 X. F. Li, J. Liu, X. L. Sun, *Energy Environ. Sci.*, 2014, **7**, 768.

7 J. Q. Zhao, Y. Wang, *Nano Energy*, 2013, **2**, 882.

8 A. K. Padhi, K. S. Nanjundaswamy, J. B. Goodenough, *J. Electrochem. Soc.*, 1997, **144**, 1188.

9 S. -Y. Chung, J. T. Blocking, Y. -M. Chiang, *Nature Materials*, 2002, **1**, 123.

10 P. S. Herle, B. Ellis, L. F. Nazar, *Nature Materials*, 2004, **3**, 147.

11 H. M. Xie, R. S. Wang, Z. M. Su, *Adv. Mater.*, 2006, **18**, 2609.

12 M. M. Thackeray, S. –H. Kong, C. S. Johnson, *J. Mater. Chem.*, 2007, **17**, 3112.

13 J. L. Liu, L. Chen, Y. Y. Xia, *J. Mater. Chem.*, 2012, **22**, 25380.

14 B. Li, H. J. Yan, W. S. Chu, Z. Y. Wu, *Adv. Funct. Mater.*, 2014, **24**, 5112.

15 X. He, J. Wang, J. Li, *Nano Research*, 2014, **7**, 110.

16 S. H, F. Felix, B. J. Hwang, *J. Am. Chem. Soc.*, 2014, **136**, 999.

17 N. Yabuuchi, K. Yoshii, S. Komaba, *J. Am. Chem. Soc.*, 2011, **133**, 4404.

18 X. K. Yang, D. Wang, X. Y. Wang, *J. Mater. Chem. A*, 2014, **2**, 3899.

19 J. M. Zheng, M. Gu, C. M. Wang, J. G. Zhang, *Nano Lett.*, 2014, **14**, 2628.

20 J. M. Zheng, M. Gu, C. M. Wang, J. G. Zhang, *Chem. Mater.*, 2014, **26**, 6320.

21 W. Zhang, Z. X. Chi, A. M, Cao, L. J. Wang, *Angew. Chem. Int. Ed.*, 2014, **53**, 12776.

22 L. J. Li, Z. Y. Chen, M. Xu, K. L. Zhang, *J. Mater. Chem. A*, 2015, **3**, 894.

23 L. N. Cong, X. G. Gao, H. M. Xie, L. Q. Sun, *Electrochimica Acta*, 2014, **115**, 399.

24 L. L. C. Guo, N. Q. Zhao, J. J. Li, C. N. He, C. S. Shi, E. Z. Liu, *ACS Appl. Mater. Interfaces*, 2015, **7**, 391.

25 C. V. Rao, A. L. M. Reddy, Y. Ishikawa, *ACS Appl. Mater. Interfaces*, 2011, **3**, 2966.

26 S. H. Ju, I. S. Kang, D. W. Kim, *ACS Appl. Mater. Interfaces*, 2014, **6**, 2546.

27 B. Qiu, J. Wang, Y. Y. Xia, Z. P. Liu, *ACS Appl. Mater. Interfaces*, 2014, **6**, 9185.

28 X. H. Liu, L. Q. Kou, L. Chen, *J. Power Sources*, 2014, **267**, 874.

29 C. Lu, H. Wu, Y. Zhang, *J. Power Sources*, 2014, **267**, 682.

30 D. H. Cho, H. Yashiro, Y. K. Sun, S. T. Myung, *J. Electrochem. Soc.*, 2014, **161**, A142.

31 L. L. Xiong, Y. L. Xu, T. Tao, *J. Mater. Chem.*, 2011, **21**, 4937.

32 Z. Y. Chen, M. Xu, Q. F. Zhao, *Applied Surface Science*, 2013, **286**, 177.

33 K. S. Park, S. B. Schougaard, J. B. Goodenough, *Adv. Mater.*, 2007, **19**, 848.

34 I. D. Scott, Y. S. Jung, S. H. Lee, *Nano Lett.*, 2011, **11**, 414.

35 G. S. Zou, X. K. Yang, X. Y. Wang, L. Ge, H. B. Shu, R. Z. Yu, *J. Solid State*

Electrochem., 2014, **18**, 1789-1797.

36 D. Liu, S. J. Clark, J. Robertson, *Applied Physics Letters*, 2010, **96**, 032905.

37 S. R. Pollack, C. E. Morris, *Journal of Applied Physics*, 1964, **35**, 1503.

38 J. Y. Kim, S. H. Kang, H. S. Kim, Y. E. Sung, *Langmuir*, 2010, **26**, 2864.

39 K. X. Wang, M. D. Wei, H. S. Zhou, J. D. Holmes, *Adv. Mater.*, 2007, **19**, 3016.

40 N. K. Yavuz, M. Herklotz, C. M. Julien, *Electrochimica Acta*, 2013, **113**, 313.

41 C. Z. Zhao, X. X. Wang, Q. Shen, *ACS Appl. Mater. Interfaces*, 2014, **6**, 2386.

42 F. Lin, I. M. Markus, M. M. Doeff, *Nature Communications*, 2014, **5**, 3529.

43 M. Gu, I. Belharouak, C. M. Wang, *ACS Nano*, 2013, **1**, 760.

44 J. L. Liu, J. Y. Liu, Y. Y. Xia, *J. Electrochem. Soc.*, 2014, **161**, A160.

45 F. Amalraj, M. Talianker, B. Markovsky, D. Aurbach, *J. Electrochem. Soc.*, 2013, **160**, A2220.

46 S. Hy, J. -H. Cheng, B. J. Hwang, *Chem. Mater.*, 2014, **26**, 6919.

47 P. Oh, M. Ko, J. Cho, *Adv. Energy Mater.*, 2014, **4**, 1400631.

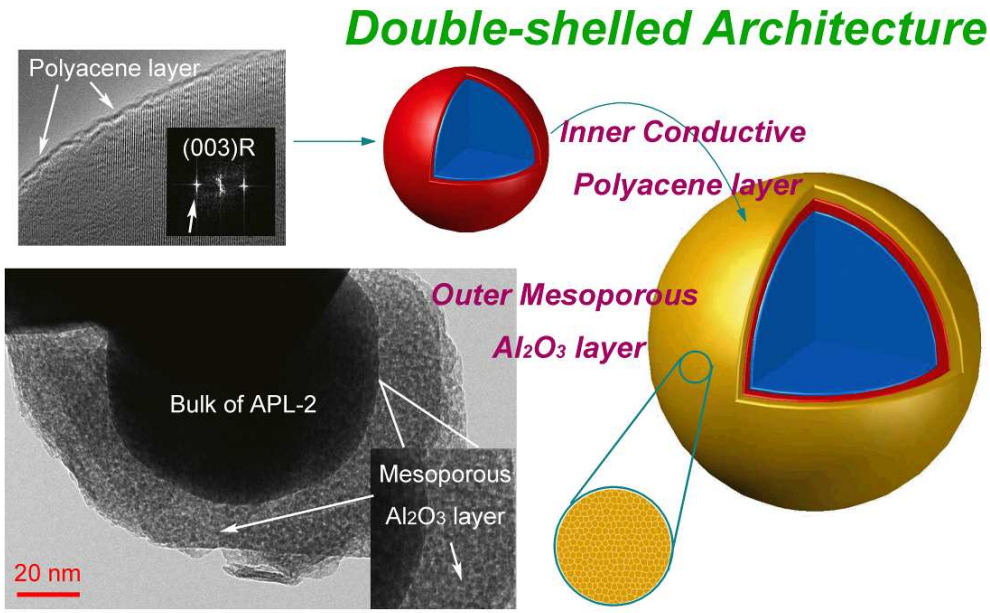

Graphic 1 Illustration of the double-shelled LLMO architecture: the inner surface with polyacene layer as high electron conductor and outer surface with highly-ordered mesoporous Al_2O_3 layer as protecting layer.